Mean flow and turbulence statistics over groups of urban-like cubical obstacles

O. Coceal · T. G. Thomas · I. P. Castro · S. E. Belcher

Abstract   Direct numerical simulations of turbulent flow over regular arrays of urban-like, cubical obstacles are reported. Results are analysed in terms of a formal spatial averaging procedure to enable interpretation of the flow within the arrays as a canopy flow, and of the flow above as a rough wall boundary layer. Spatial averages of the mean velocity, turbulent stresses and pressure drag are computed. The statistics compare very well with data from wind-tunnel experiments. Within the arrays the time-averaged flow structure gives rise to significant 'dispersive stress' whereas above the Reynolds stress dominates. The mean flow structure and turbulence statistics depend significantly on the layout of the cubes. Unsteady effects are important, especially in the lower canopy layer where turbulent fluctuations dominate over the mean flow.

1 Introduction

Our understanding of the structure and dynamics of turbulent boundary layers on aerodynamically smooth walls has been clarified over the last ten years or so (see Hamilton et al. 1995; Jimenez and Pinelli 1999). However, the dynamics of turbulent boundary layers over rough surfaces is much less well known, as emphasised in the recent review by Jimenez (2004). Nevertheless there are many applications that require understanding of the mean flow and turbulence both above and within a canopy of roughness elements, for example atmospheric boundary-layer flows over surfaces that are vegetated or covered with buildings (Britter and Hanna 2003;

O. Coceal (✉) · S. E. Belcher
Department of Meteorology, University of Reading, PO Box 243, Reading RG6 6BB, UK
e-mail: o.coceal@reading.ac.uk

T. G. Thomas · I. P. Castro
School of Engineering Sciences, University of Southampton, Southampton SO17 1BJ, UK

Coceal and Belcher 2004). In these cases, it is important to understand the mixing and transport processes in the boundary layer above the canopy of roughness elements, within the canopy and also the coupling between these parts of the flow.

Here we begin to address these questions by performing direct numerical simulations of boundary-layer flow over surfaces covered with regular arrays of cubes. There exist both laboratory and direct numerical simulations for two-dimensional roughness consisting of square bars (Djenidi et al. 1999; Leonardi et al. 2003). Cheng and Castro (2002) and Castro et al. (2006) recently performed careful wind-tunnel measurements over three-dimensional, cubical obstacles. However, well-resolved numerical simulations over this geometry have not been performed before with demonstrated credibility. In the present work the Navier–Stokes equations are integrated without any tuning or modelling assumptions, for conditions when the boundary-layer flow is in the high Reynolds number turbulent regime. The flow around individual cubes is well resolved.

The first aim of the present paper then is to establish the fidelity of the simulations through numerical tests and comparisons with wind-tunnel measurements. The second aim of this paper is to analyse the results within the canopy framework (Belcher et al. 2003): the flow is analysed by taking time and spatial (volume) averages of flow quantities (Raupach and Shaw 1982; Raupach et al. 1991; Finnigan 2000). Here we are specifically interested in the terms of the spatially-averaged momentum budget. A third aim is to investigate how the mean flow structure and the turbulence statistics depend on the layout of the roughness array. Such information is important in helping modellers decide how best to model urban areas.

2 Background

The spatial averaging formalism has been exploited in the literature on plant canopy flows (Raupach and Shaw 1982; Finnigan 1985, 2000). It is a natural way to treat flows over rough surfaces that are spatially inhomogeneous. The averaging volume is taken to be very thin in the vertical, and large enough in the horizontal directions to eliminate flow variations due to individual obstacles. Prognostic variables, such as velocity component u_i, may then be decomposed into three components

$$u_i = U_i + \tilde{u}_i + u_i', \tag{1}$$

where $U_i = \langle \overline{u}_i \rangle$ is the time and space averaged velocity, referred to here as the mean velocity, $\tilde{u}_i = \overline{u}_i - U_i$ is the spatial variation of the time mean flow and $u_i' = u_i - U_i - \tilde{u}_i$ is the turbulent fluctuation; the overbar denotes a time average and angle brackets denote a spatial average. Applying time and spatial averaging to the momentum equations then yields the spatially-averaged momentum equation, valid at each height z (Finnigan 2000)

$$\frac{\partial \langle \overline{u}_i \rangle}{\partial t} + \langle \overline{u}_j \rangle \frac{\partial \langle \overline{u}_i \rangle}{\partial x_j} = -\frac{\partial \langle \overline{p} \rangle}{\partial x_i} + \frac{\partial \tau_{ij}}{\partial x_j} + D_i \tag{2}$$

where

$$\tau_{ij} = -\overline{\langle u_i' u_j' \rangle} - \langle \tilde{u}_i \tilde{u}_j \rangle + \nu \frac{\partial \langle \overline{u}_i \rangle}{\partial x_j}, \tag{3a}$$

$$D_i = \frac{1}{V} \int_S \overline{p}\, n_i\, dS - \frac{\nu}{V} \int_S \frac{\partial \overline{u}_i}{\partial n}\, dS. \tag{3b}$$

Here V is the volume occupied by the fluid, S is the surface area of the obstacles within the averaging volume, n_i is the unit normal pointing from S into V, and ν is the kinematic viscosity. We use units in which the density of air $\rho = 1$. The spatially-averaged stress tensor τ_{ij} consists of the usual Reynolds stress and viscous stress as well as the *dispersive stress* $\langle \tilde{u}_i \tilde{u}_j \rangle$. The dispersive stress represents transport of momentum by spatial variations in the horizontal plane. Within the canopy volume, the drag term D_i consists of the sum of the *form drag* and the *viscous drag* (which is found to be negligibly small in the present computations). Under conditions of stationarity and homogeneity, the terms on the left-hand side of Eq. (2) vanish, and hence the sum of the stress gradient and drag force must balance any applied pressure gradient. The objective is then to quantify the contributions of the various terms to the stress and drag in Eq. (3) and to investigate their dependence on the roughness geometry.

3 Numerical approach

3.1 Model description and domain set-up

The Navier–Stokes equations are discretised using second-order central finite differences in space and a second–order Adams–Bashforth scheme in time, based on the pressure correction method. The code is parallelized in a highly efficient manner and a flexible multi-block mapping strategy is developed to deal with the flow domain containing the complex geometry. Based on these, the Poisson equation for pressure p is solved by a multigrid method. For further details of numerical methods see Yao et al. (2001).

Figure 1 shows a plan view of the computational domains in the different runs. A total of seven runs were performed, as summarised in Table 1. The runs are code-named in the form *LWH-R*, where L, W and H are the streamwise, lateral and vertical dimensions of the domain as a multiple of the cube height h, and R denotes the resolution in terms of number of grid points per cube. A Cartesian constant spacing and isotropic grid is used throughout the domain, with grid size Δ. As a test of grid resolution three runs 444-16, 444-32 and 444-64 were performed with a staggered array and had $\Delta = h/16, h/32, h/64$, respectively. Two further runs 446-32 and 884-32, again in staggered configuration, were compared with 444-32 to investigate any possible influence of domain height and horizontal extent on computed statistics. Finally, two runs 444A-32 and 444S-32 were done with arrays in aligned and square configurations, respectively (see Fig. 1 for definitions of 'staggered', 'aligned' and 'square' arrays). The notational convention adopted is that x, y and z denote the streamwise, lateral and vertical coordinates, and that u, v and w denote the streamwise, lateral and vertical components of velocity, respectively.

Periodic boundary conditions are imposed both laterally and streamwise to simulate an infinite array. The boundary condition at the top of the domain is free slip. No-slip and impermeability boundary conditions are applied at the bottom and on all obstacle surfaces. The flow is maintained by a height-independent streamwise pressure gradient of magnitude u_τ^2/H, where u_τ is the total wall friction velocity. The Reynolds number of the flow, based on the velocity at the top of the domain and the cube height, is $Re = 5,000$. The roughness Reynolds number $R_\tau \equiv u_\tau h/\nu = 500$, which is in the fully rough regime. Cheng and Castro (2002) performed wind-tunnel measurements over the same geometries at a Reynolds number of $Re = 5000$, based on the
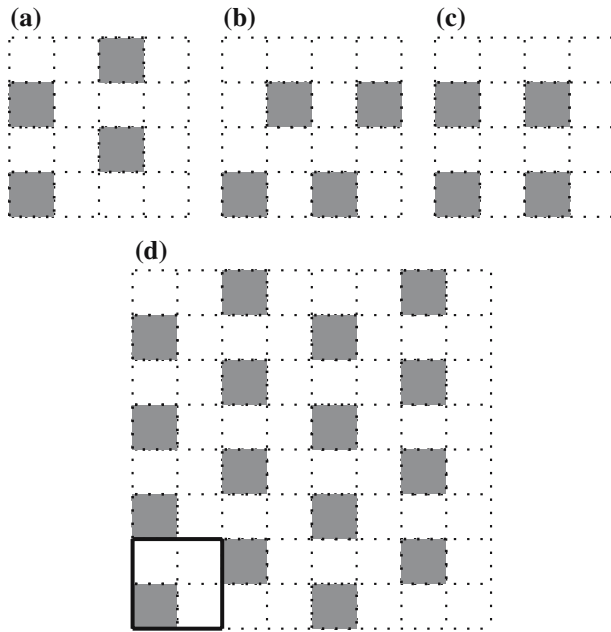
Fig. 1 Plan view of computational domains. (**a**) to (**c**): staggered, aligned and square arrays of dimensions $4h \times 4h \times 4h$, where h is the cube height. (**d**) wider domain in staggered arrangement ($8h \times 8h \times 4h$), also indicating a 'repeating unit' (bold lines). An additional run was performed with taller domain $4h \times 4h \times 6h$ for the staggered configuration. The streamwise direction in all cases is left to right

Table 1 Summary of runs performed. For definitions of 'staggered', 'aligned' and 'square' arrays, see Fig. (1). Here L, W and H are the streamwise, lateral and vertical dimensions of the domain, respectively, and h is the height of the cube

Run	Layout	L	W	H	Gridpoints per cube	Gridpoints total
444-16	Staggered	$4h$	$4h$	$4h$	$16 \times 16 \times 16$	$64 \times 64 \times 64$
444-32	Staggered	$4h$	$4h$	$4h$	$32 \times 32 \times 32$	$128 \times 128 \times 128$
444-64	Staggered	$4h$	$4h$	$4h$	$64 \times 64 \times 64$	$256 \times 256 \times 256$
446-32	Staggered	$4h$	$4h$	$6h$	$32 \times 32 \times 32$	$128 \times 128 \times 192$
884-32	Staggered	$8h$	$8h$	$4h$	$32 \times 32 \times 32$	$256 \times 256 \times 128$
444A-32	Aligned	$4h$	$4h$	$4h$	$32 \times 32 \times 32$	$128 \times 128 \times 128$
444S-32	Square	$4h$	$4h$	$4h$	$32 \times 32 \times 32$	$128 \times 128 \times 128$

free-stream velocity and the cube height and with a boundary-layer height $\delta \approx 7.5h$. Their roughness Reynolds number was $R_\tau \equiv u_\tau h / \nu = 343$. For sharp-edged obstacles, the dependence of the flow on Reynolds number is weak (Castro and Robins 1977; Snyder and Castro 2002) and indeed Cheng and Castro (2002) found that there was very little variation in the drag coefficient between $Re \approx 5000$ and $Re \approx 12000$.

3.2 Integration times

To ensure temporal convergence to a statistically steady state, all the simulations were run for an initial duration of about $200T$, where $T = h/u_\tau$ is an eddy turnover time

for the largest eddies shed by the cubes. Statistics were then collected and averaged over a further duration of $400T$ to ensure statistical convergence. The timestep used in the simulations was $0.00025T$ at the resolution $\Delta = h/32$ and $0.000125T$ at the resolution $\Delta = h/64$. Therefore, statistics were summed over a total number of 1.6 million timesteps for $\Delta = h/32$ and 3.2 million timesteps for $\Delta = h/64$ sampling every 20 timesteps in either case. The importance of using such a long averaging time is explained in Section 4.3.

The large number of grid points (16.8 million for run 444-64), small timestep and long integration time required substantial supercomputing resources even with the highly efficient code used. Each of the runs was performed on 30 or 60 processors on an SGI Altix supercomputer. The highest run 444-64 alone took about 800 hours per processor running on 60 processors on an SGI Altix 3700 supercomputer, or an equivalent total of 48000 single processor cpu hours.

3.3 Numerical tests

3.3.1 Grid resolution requirements

A well-resolved simulation needs to capture all the dynamically relevant turbulence scales down to dissipation scales. These dissipation scales may be estimated as follows. Assuming that production is approximately equal to dissipation, the dissipation rate may be estimated as $\epsilon \approx u_*^2 \partial u/\partial z$, where u_*^2 is here defined as the value of the Reynolds stress at $z = h$. In the canopy flow, the numerical results give $\partial u/\partial z \approx 2.5u_*/h$, hence $\epsilon \approx 2.5u_*^3/h$, giving a Kolmogorov length scale $\eta \equiv (\nu^3/\epsilon)^{1/4} \approx 0.0075h$. This gives $\eta \approx 0.5\Delta$ for $\Delta = h/64$ and $\eta \approx 0.25\Delta$ for $\Delta = h/32$. In the shear layer at the top of the array the maximum values of $\epsilon \approx 34u_*^3/h$ (as implied by the numerical results), giving $\eta \approx 0.0039h$, which is $\approx 0.25\Delta$ for $\Delta = h/64$ and $\approx 0.125\Delta$ for $\Delta = h/32$. Hence, the grid size Δ lies between 2η and 4η for the highest resolution run 444-64 and between 4η and 8η for the standard resolution runs. As pointed out by Moin and Mahesh (1998), the smallest length scale that must be resolved depends on the energy spectrum and is typically greater than the Kolmogorov length scale η. For example in curved channel flow most of the dissipation occurs at scales greater than 15η (Moin and Mahesh 1998), whereas a computation based on the Pao spectrum (Pao 1965) gives a threshold of 11η. Hence, the present simulations capture the major part of the dissipation spectrum and are therefore well-resolved based on this criterion.

3.3.2 Grid resolution tests

The sensitivity of the spatially averaged results to grid resolution is shown in Figs. 2a and b, which plot vertical profiles of the spatially averaged total stress component $\tau_{13}(z)$ and of the mean wind speed $U(z)$ computed for runs 444-64, 444-32 and 444-16. There is close agreement between the results for runs 444-32 and 444-64. Figure 2a shows that the computed stress is almost identical at these two resolutions. The mean velocity computed in the two runs also agrees very well especially within and just above the array; the maximum difference occurs at the top of the domain, and is about 6% there. A direct test of convergence of the finest grid used in run 444-64 could not be performed but in terms of the statistics of interest in this paper, a doubling of the highest grid resolution would give an estimated agreement with 444-64 to within about 1% (based on a Richardson extrapolation). The run 444-64 took about
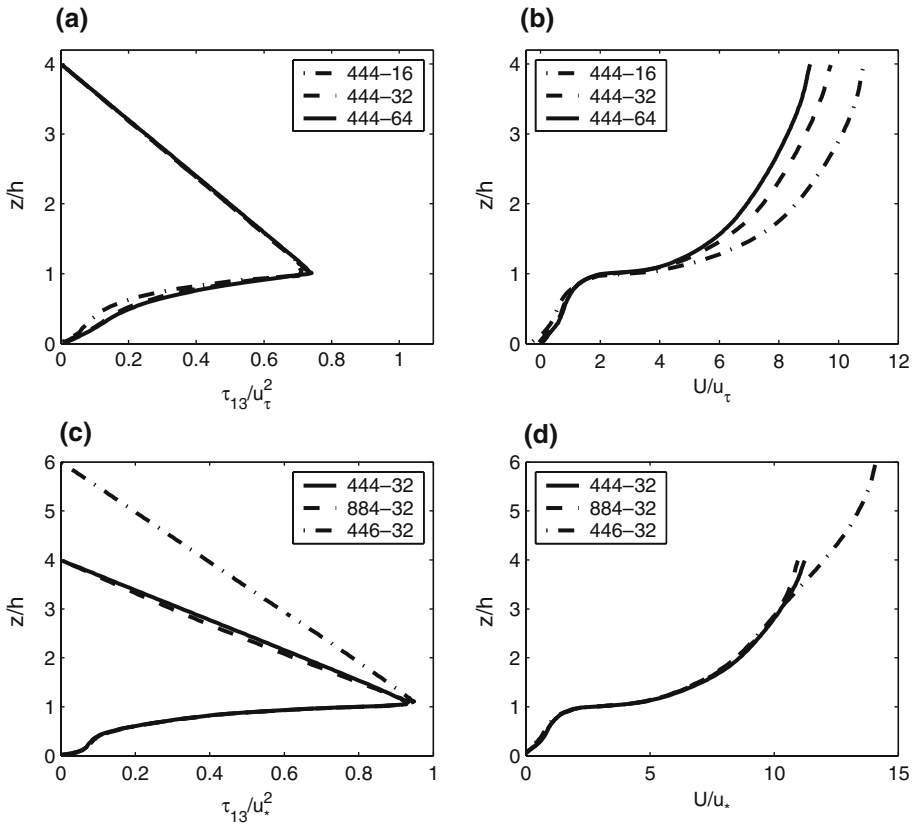
Fig. 2 (**a**) and (**b**): Effect of grid resolution on computed statistics (results normalised using u_τ). (**c**) and (**d**): Effect of domain size on computed statistics (results normalised using u_*)

48000 single processor cpu hours on an SGI Altix 3700 supercomputer. Clearly there is little to gain from the enormous extra computational time that a further doubling of the grid resolution would require. The results of the 444-64 run are compared against wind-tunnel data in the following sections, and they show very good agreement.

The lowest resolution run 444-16 gives rather large errors. Hanna et al. (2002) and very recently Kanda et al. (2004) performed large-eddy simulation (LES) over groups of cubes with a resolution of only 10 gridpoints per cube. There were discrepancies of up to 40% in the comparisons of the LES of Hanna et al. (2002) with wind-tunnel data, whereas Kanda et al. (2004) showed little quantitative comparison with data. Stoesser et al. (2003) also recently performed LES of flow over multiple cubes but at a better resolution of 25 gridpoints per cube. Although they had only one cube in the domain (applying periodic boundary conditions), they showed that mean velocity and stress profiles agreed very well with observations. They also found that switching off the subgrid-scale model had virtually no effect on the results. We conclude that simulations over this type of geometry are generally well resolved by $\Delta \approx h/32$, at least at the present Reynolds number.

🖉 Springer

3.3.3 Domain size tests

Figures 2c and d show the effect of changing the domain size by plotting profiles from runs 444-32, 884-32 and 446-32. In Fig. 2c, the stress profiles have been non-dimensionalised by u_* because the stress profile differs in the taller domain of run 446-32. The profiles for 884-32 and 444-32 collapse onto each other, indicating that the smaller domain in run 444-32 is adequate. For run 446-32 the stress profile within the array also collapses onto the other two. Similarly, the mean wind profile is in excellent agreement up to about $z = 3.5h$, and indicates that the limited domain height for the runs with domain height $4h$ does not constrain the flow below $z = 3.5h$.

These results demonstrate that the mean flow and turbulence statistics can be captured accurately with even a relatively small domain size, by exploiting the regularity of the geometry with the application of periodic boundary conditions in the horizontal directions. Larger domains would inevitably be necessary if one were interested in capturing unsteady large-scale organised structures such as those reported recently in the LES work of Kanda et al. (2004). However, since the present study focuses on the mean flow, horizontally-averaged turbulent statistics and small-scale turbulent structures, the domain size limitations pose no problems here.

4 Results and discussion

4.1 Unsteady flow visualisation

Whilst the main interest of this paper is in the statistics of the flow integrated over a long time, it is instructive to begin by looking at instantaneous snapshots of the flow. Such information is difficult to obtain by other means and provides valuable insights into the nature of fully developed turbulent flow over complex urban-type geometry.

4.1.1 The velocity field

Figure 3 shows an instantaneous snapshot of the velocity field for the staggered array over part of the domain for the highest resolution run $444 - 64$. The very fine grid used here, wherein each unit cube is resolved by 64^3 gridpoints, reveals flow features in unprecedented detail. Wind vectors (v, w) are plotted in a vertical $y - z$ plane through the middle of the cubes shown. The mean flow is out of the page. The instantaneous flow pattern is much more complex than that of the mean flow (compare with Fig. 18). The wind field is strongly inhomogeneous, especially below about $z = 2h$, and vortical structures are present throughout the flow. Fig. 4 shows in greater detail the region around the top of the cubes and Fig. 5 shows the region between the cubes. Vortical structures can distinctly be seen with associated streamwise circulation in both clockwise and anticlockwise sense. Such features of the unsteady flow have not been seen before at this level of detail in either numerical or wind-tunnel simulations.

A snapshot of the velocity field in a streamwise-vertical $(x - z)$ plane is shown in Fig. 6. Wind vectors (u, w) are plotted in a slice through the middle of the cube shown. The mean flow is to the right. The plot is shown at half resolution for greater clarity. Organised features are evident here also. The most obvious ones are the darker regions lying approximately between $z = h$ and $z = 2h$. Most of these are associated with
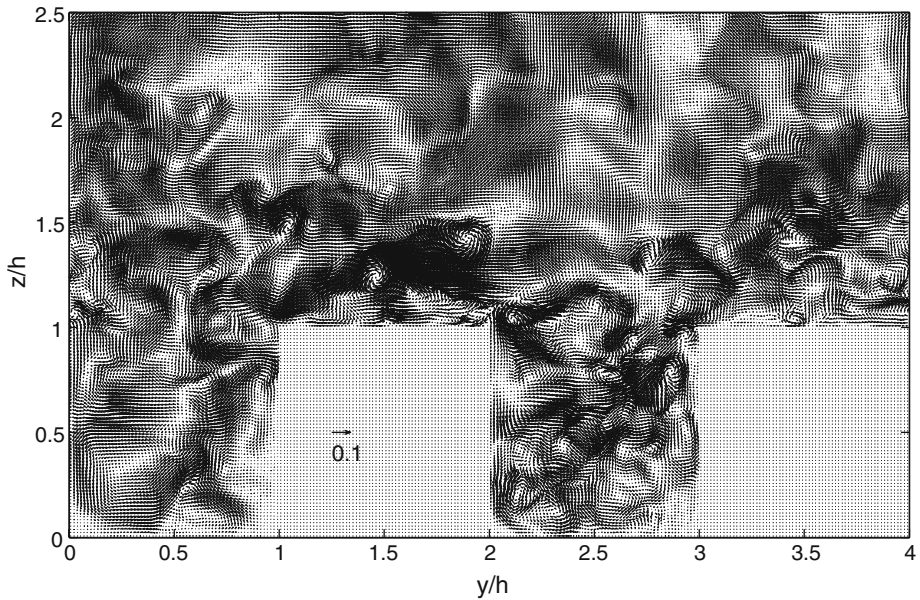
Fig. 3 An instantaneous snapshot of the velocity field over the staggered array shown in unprecedented detail. Wind vectors (v, w) are plotted in a vertical $y - z$ plane through the middle of the cubes shown. In this and subsequent velocity vector plots, the inserted arrow indicates the scale of the velocity vectors (given value is velocity magnitude normalised by u_τ). The mean flow is out of the page. Note the complexity of the instantaneous flow pattern
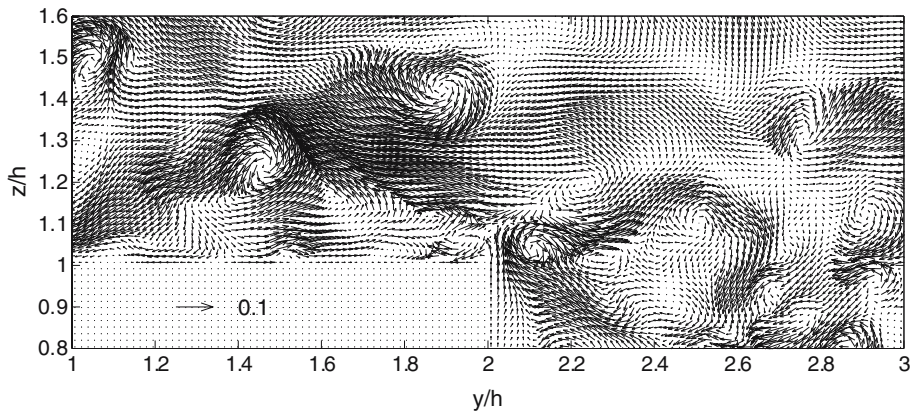
Fig. 4 As in Fig. 3 showing in greater detail the region around the top of the cubes. Note the presence of vortical structures rotating in both a clockwise and anticlockwise sense

large streamwise velocity components and downward vertical velocity components. Such motions are known as 'sweeps' and, together with 'ejections', are effective means of downward momentum transport.
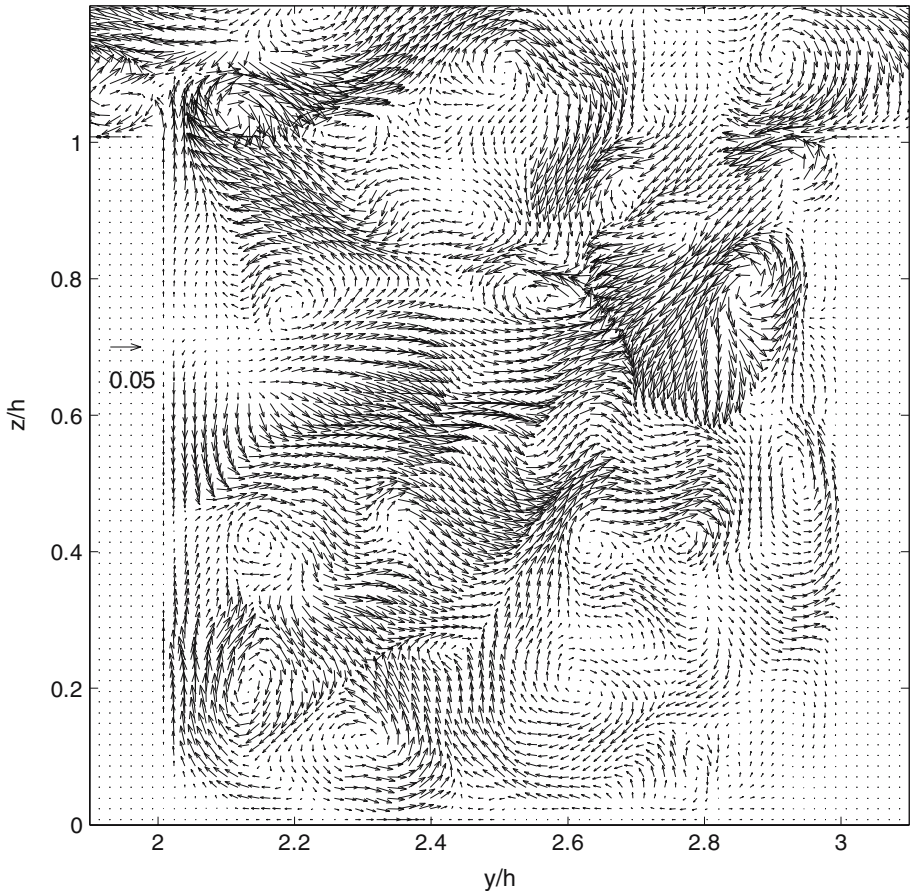
Fig. 5 As in Fig. 3 showing in greater detail the region between the cubes. The very fine grid (each unit cube is resolved by 64^3 gridpoints) allows flow features to be resolved within the roughness array to an extent not seen before in either numerical or laboratory simulations
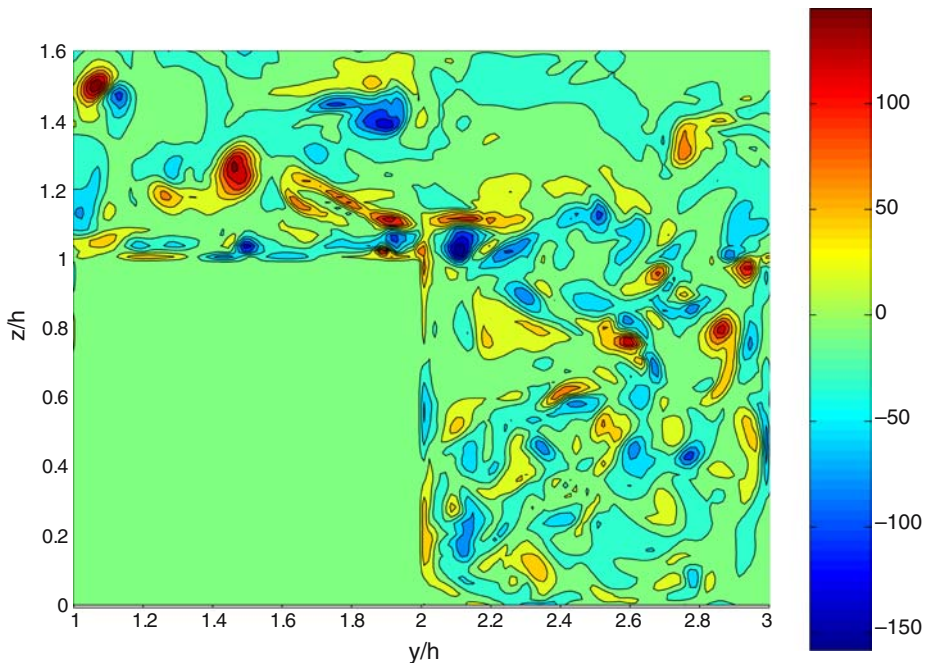
4.1.2 The vorticity field

Figure 7 shows contours of streamwise vorticity ω_x corresponding to the snapshot shown in Fig. 3 and plotted in the same plane ($y - z$) around the middle cube (the mean flow is out of the paper). Several regions of positive and negative vorticity appear in pairs, and correspond to the counter rotating wind vector patterns identified in Figs. 4 and 5. Many of these vortical structures are the legs of so-called hairpin vortices. These vortices are responsible for generating the strong sweeps and ejections mentioned above and hence most of the Reynolds shear stress (Coceal et al., submitted). The present simulations are able to explicitly resolve actual turbulent structures like these at all dynamically relevant scales. Hence, it is important to realise that the computed flow statistics are not modelled as in other numerical approaches such as RANS, but result from explicit computation of directly resolved turbulence.
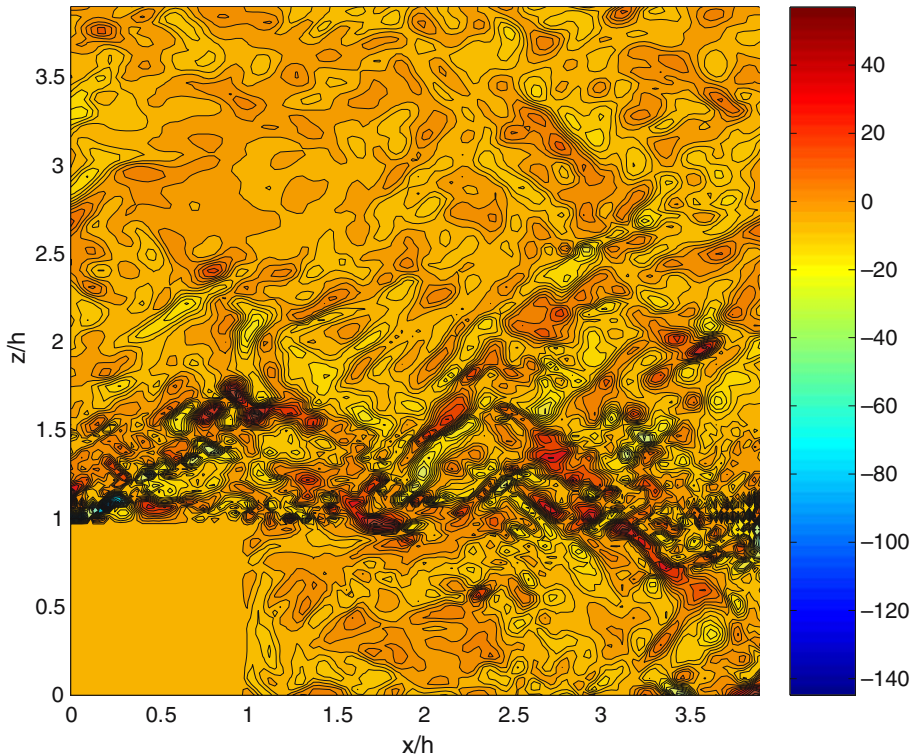
   Figure 8 shows contours of spanwise vorticity ω_y corresponding to the snapshot shown in Fig. 6 and plotted in the same vertical $x - z$ plane through the middle of
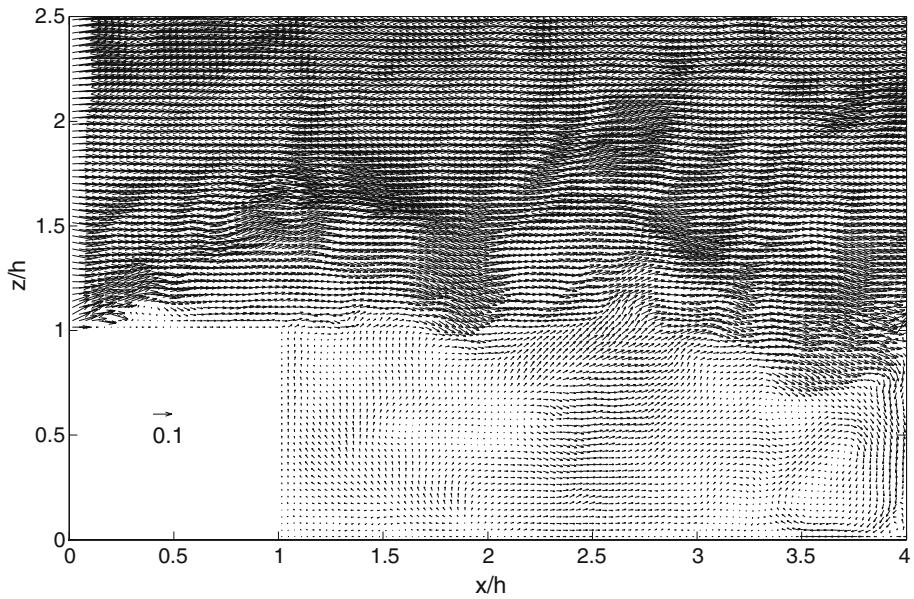
Fig. 6 Instantaneous snapshot of the velocity field over the staggered array showing wind vectors (u, w) plotted in a vertical $x - z$ plane through the middle of the cube shown. The mean flow is to the right. The plot is shown at half resolution for greater clarity

Fig. 7 Contours of streamwise vorticity ω_x corresponding to the snapshot shown in Fig. 3 and plotted in the same plane $(y - z)$ around the middle cube. Values of vorticity shown on colour bar are normalised by u_τ / h. Several regions of positive and negative vorticity appear in pairs

Fig. 8 Contours of spanwise vorticity ω_y corresponding to the snapshot shown in Fig. 6 and plotted in the same vertical $x - z$ plane through the middle of the cube shown. Values of vorticity shown on the colour bar are normalised by u_τ/h. This shows the presence of a strong shear layer over the top of the cubes

the cube shown (but to a different scale). A region of concentrated spanwise vorticity can be seen just over the top of the cube and stretching out to the next cube (which is just outside the bottom right of the domain, from $x/h = 4$ to $x/h = 5$). This region of high vorticity corresponds to the presence of a strong shear layer, with high values of wind shear $\partial u/\partial z$. A sequence of such snapshots (not shown) reveals that this strong shear layer is persistent over extended periods of time. Hence, it is very likely to play an important part in the coupling of turbulent motions within the canopy with larger scale boundary-layer eddies.

The coherent aspects of the unsteady flow and their statistical properties are studied in detail elsewhere (Coceal et al., submitted). The rest of the present paper looks at the mean flow structure and statistics over a large integration time, and the spatial average over the flow domain of these long time mean statistics.

4.2 Time-mean flow

4.2.1 Mean flow structure

A sequence of snapshots of the flow field such as those shown in the last section shows that the flow at the simulated Reynolds number is highly unsteady and departs

(a)

(b)
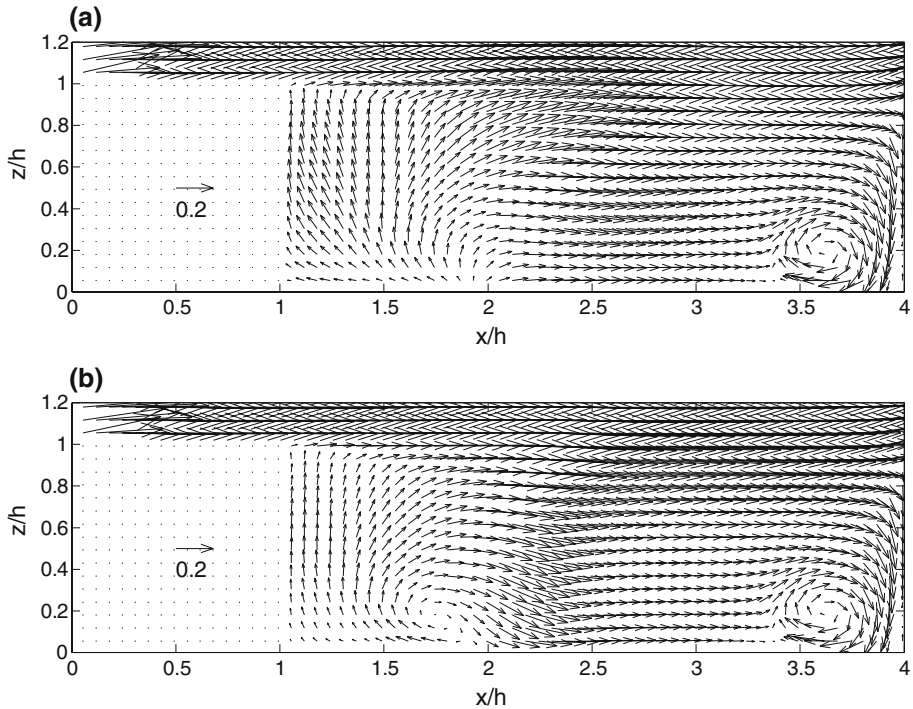
Fig. 9 (**a**) Mean flow structure in a vertical $x − z$ plane through the middle of the cube in the staggered array showing (u, w) wind vectors. (**b**) Similar plot in a vertical $x − z$ plane parallel to the one above and at distance of $0.25h$ away. Note that the wind vectors are plotted every four grid points for greater clarity

significantly from the mean flow. Yet, the structure of the time-mean flow is important because it determines the pressure drag and the dispersive stress.

Figure 9a shows (u, w) wind vectors in a vertical $x − z$ plane through the middle of the cube in the staggered array, and is the long time-mean version of Fig. 6. In this and subsequent plots, wind vectors are plotted at reduced resolution for greater clarity. The most obvious feature in 9a is a recirculation in front of the cube, in the bottom right-hand corner. Associated with this vortex is a strong downdraft down the front face of the cube. This vortex is a robust feature of the flow; it is seen to be quite persistent in a long time sequence of snapshots such as Fig. 6.

A less obvious feature of Fig. 9a is the absence of a recirculation behind the cube. There is reverse flow near the bottom surface between $x/h = 1$ and $x/h = 2$, but nothing resembling a vortex that one might have expected to see based on experience with two-dimensional flows in street canyons (see for example Cui et al. 2004). There is a strong updraft adjacent to the back face of the cube. Figure 9b shows how the picture changes in a vertical $x − z$ plane parallel to the one above and at distance of $0.25h$ away, so that it is off the axis of symmetry. There is now a recirculating vortex in the lower part of the canopy between $x = 1.5h$ and $x = 2h$. These two plots taken together illustrate the strong three-dimensionality of the flow.

Additional insight is gained by looking at the mean flow pattern in a horizontal plane. Figure 10 shows a wind vector plot of the mean wind field (u, v) in an $x − y$ plane
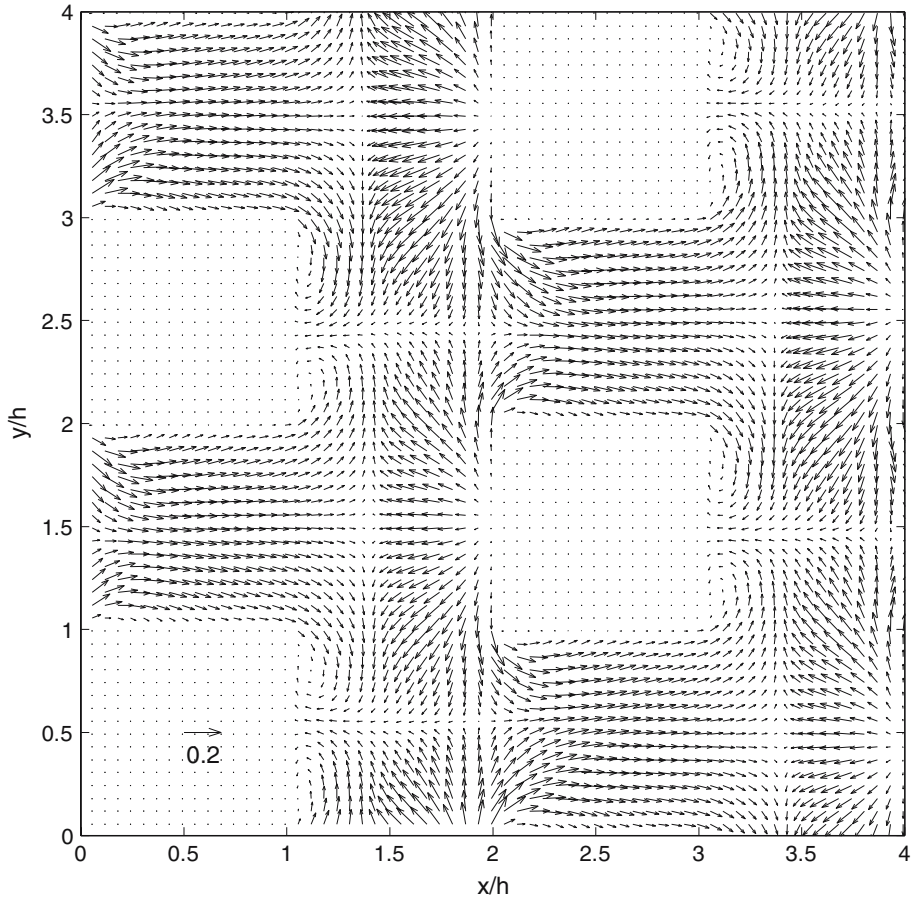
Fig. 10 Wind vector plot of the mean wind field (u, v) in a horizontal $x - y$ plane close to the bottom surface at $z = 0.05h$ in the staggered array

close to the bottom surface at $z = 0.05h$ in the staggered array. Here we see strong reverse flow from the front faces of the cubes. In this plane, there is also a lateral convergence of wind vectors behind the cubes onto their centrelines such as $y = 2.5h$. Because this plane is close to the bottom surface, continuity dictates that there should be an updraft in the vertical planes through those centrelines, and this can be seen in Figure 9a. The picture changes further up in the canopy. Figure 11 shows the (u, v) wind vector pattern in the $x - y$ plane at $z = 0.5h$ (half the cube height). At this height there is no reverse flow from the front faces of the cube. Note the clear effect of flow separation on the side walls of the cubes in diverting high momentum fluid towards the middle of the gap between cubes. One can also see a recirculating vortex pair behind the cube, similar to the pattern behind an isolated cube (Martinuzzi and Tropea 1993).

Figures 12–14 show the mean flow structure for the square array corresponding to the same planes as in Figures 9, 10 and 11 respectively. The alignment of the cubes and the fact that cubes in each row are now much closer together (being separated
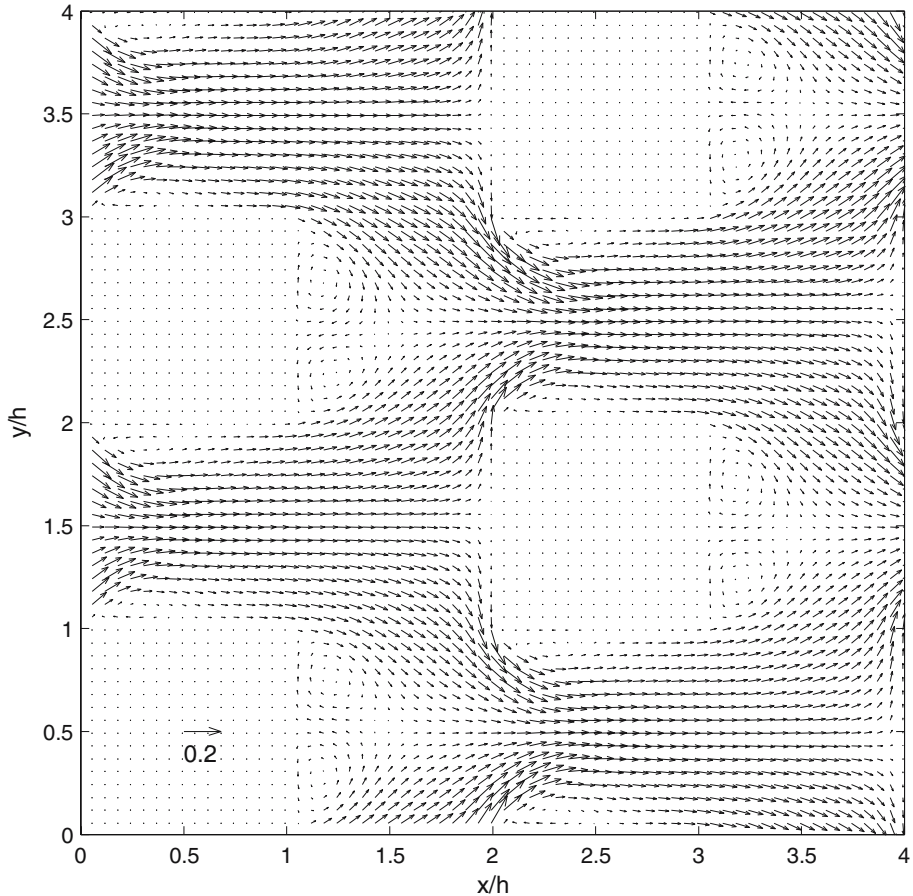
Fig. 11 Similar to Fig. 10 in a horizontal $x - y$ plane at $z = 0.5h$ (half the cube height)

by a gap of length h as compared to $3h$ in the staggered case) result in a completely different mean flow pattern. Figure 12 shows that the mean flow behind the cubes is now dominated by a large recirculation, and this is true even in vertical $x - z$ planes off the axis of symmetry. This flow pattern is qualitatively similar to that over a two-dimensional street canyon (Cui et al. 2004). Figure 13, in the $x - y$ plane at $z = 0.05h$, shows a much simpler flow structure than the corresponding plot for the staggered array, Fig. 9. There is basically fast flow in the unobstructed region between rows of cubes and strong reverse flow in the region between successive cubes within the rows. Figure 14 shows that the counter-rotating vortex pair in the $x - y$ plane at $z = 0.5h$ is now larger and spans the whole region between successive cubes.

In conclusion the results of this section illustrate important differences between three-dimensional flows and flows through cube layouts that are more closely two dimensional. They illustrate the risks of thinking based upon typically two-dimensional street canyon-type flows in situations where building arrangements may be more three-dimensional. The flow topology in the two cases is very different (Tobak and Peake 1982) and, as Delery (2001) points out, even the vocabulary used to describe

(a)

(b)
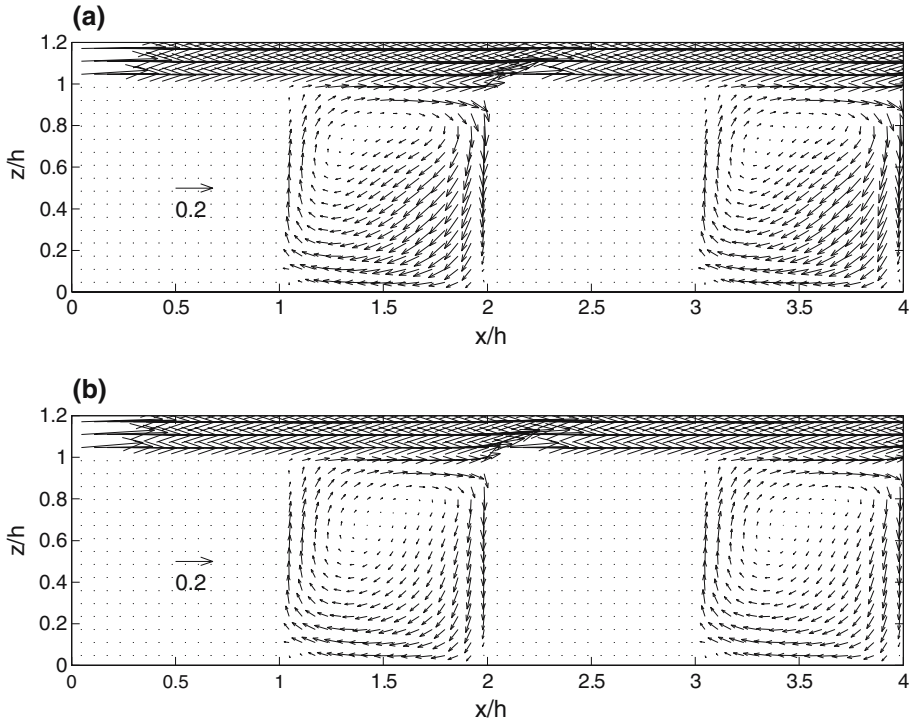
Fig. 12 (**a**) Mean flow structure in a vertical $x - z$ plane through the middle of the cube in the aligned array showing (u, w) wind vectors. (**b**) Similar plot in a vertical $x - z$ plane parallel to the one above and at distance of $0.25h$ away

two-dimensional flows may not be appropriate for more complex three-dimensional flows. Belcher (2005) discusses the effect of street intersections such as four-way junctions and T-junctions on dispersion. A careful study of the flow topology in such cases would help to understand the patterns of mixing and transport.

4.2.2 Mean flow statistics

Computed mean flow statistics are now compared with the wind-tunnel measurements of Cheng and Castro (2002). Figure 15a shows the vertical profile of laterally integrated pressure difference between front and back faces of a cube in the staggered array, normalised by the pressure difference in the middle, $\int (p_f - p_b)\, dy / \Delta p_m$. The experimental data were obtained from an array of 42 pressure tappings placed on both front and back faces of a cube (Cheng and Castro 2002). The computed profile is in excellent agreement with the measurements.

Figure 15b shows a wind vector plot of mean u, v at $z = 0.1h$ in a 'repeating unit' of the staggered array. Figures 15c–f plot the vertical profiles of mean streamwise velocity u over four locations corresponding to respective coordinate positions $(0.5, 1.5)$, $(0.5, 0.5)$, $(1.5, 1.5)$ and $(1.5, 0.5)$ in Figure 15b. The circles in those plots are data points from the measurements of Cheng and Castro (2002). Note the negative velocities near the bottom in Figures 15e and f, as also reflected in the wind vectors at
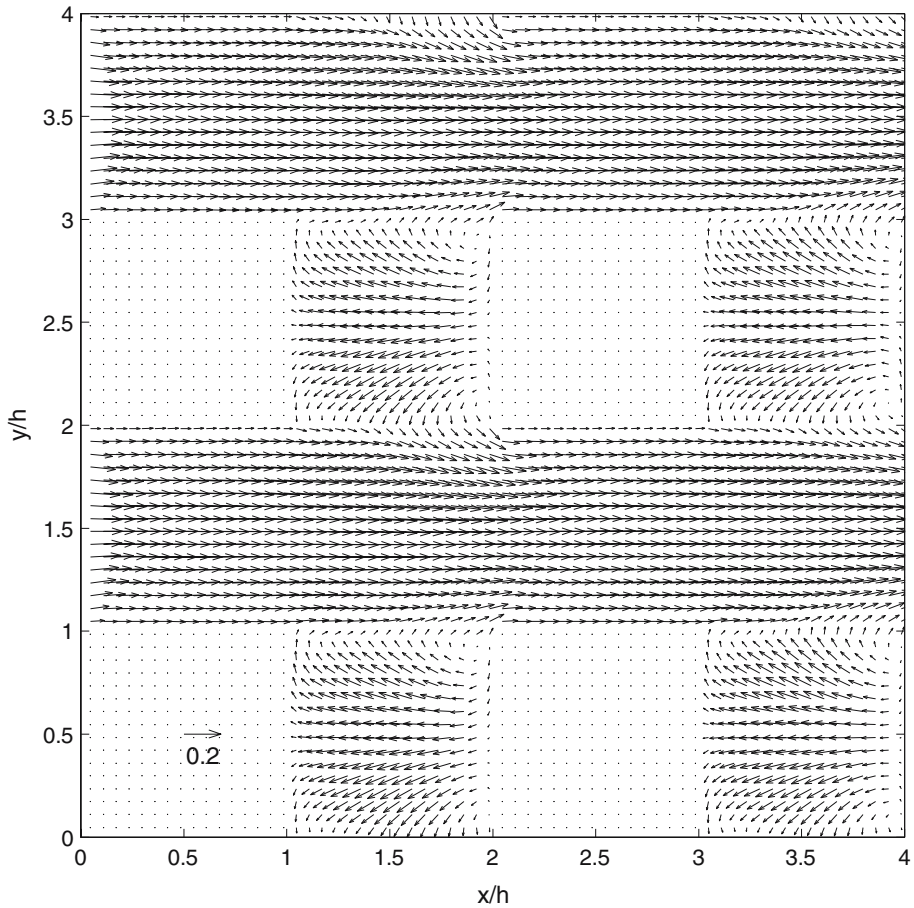
Fig. 13 Wind vector plot of the mean wind field (u, v) in a horizontal $x - y$ plane close to the bottom surface at $z = 0.05h$ in the aligned array

the corresponding locations $(1.5, 1.5)$ and $(1.5, 0.5)$. The computed profiles agree very well with the data both within the array and above.

Further statistics are presented in the next section as spatial averages over the flow domain.

4.3 Spatially-averaged mean flow

### 4.3.1 Reynolds and dispersive stresses

Figure 16 shows the computed spatially-averaged Reynolds and dispersive stresses, compared with wind-tunnel measurements made above the staggered and aligned arrays by Cheng and Castro (2002). Figure 16a plots the r.m.s. values $\langle \overline{u'w'} \rangle^{1/2}$, $\langle \overline{u'^2} \rangle^{1/2}$ and $\langle \overline{w'^2} \rangle^{1/2}$ for the staggered array and Figure 16b plots the same quantities for the aligned array. Cheng and Castro (2002) made 25 profile measurements above the aligned array, and this allowed them to compute reliable values for the dispersive
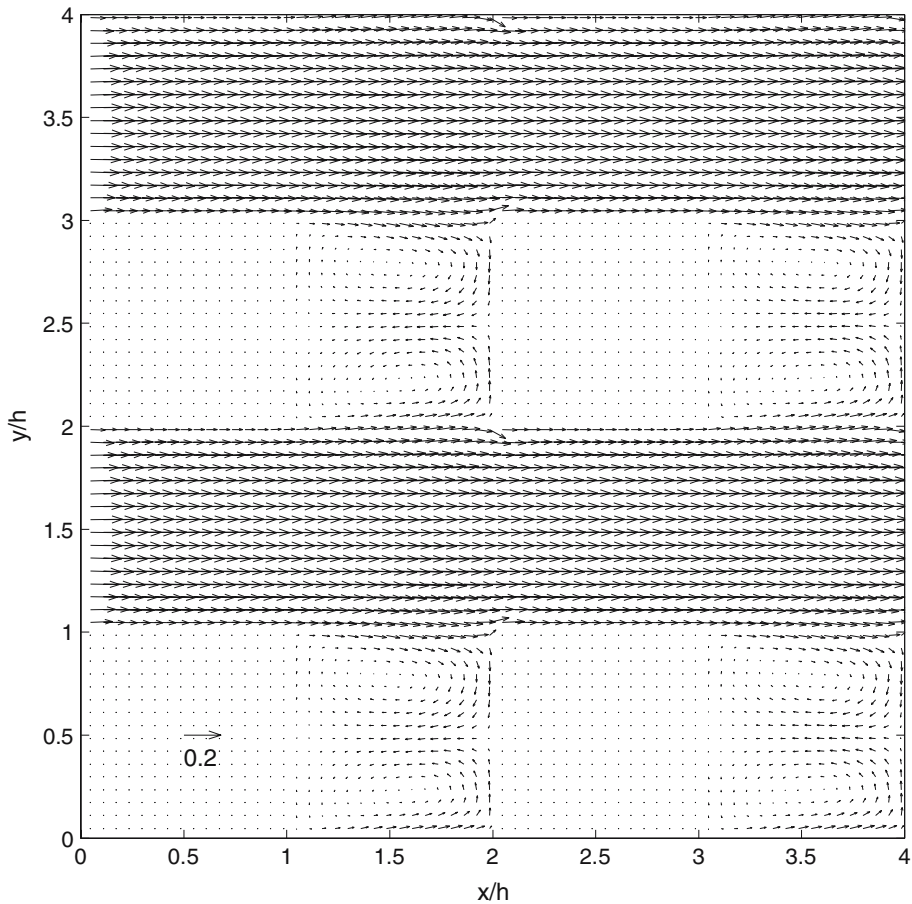
Fig. 14 Similar to Fig. 13 in a horizontal $x - y$ plane at $z = 0.5h$ (half the cube height)

stresses. Figure 16c compares the computed r.m.s. values $\langle \tilde{u}\tilde{w}\rangle^{1/2}$, $\langle \tilde{u^2}\rangle^{1/2}$ and $\langle \tilde{w^2}\rangle^{1/2}$ with the measurements. In these plots, the stresses have been normalised by u_*^2 while distances have been scaled by $(z - d)/D$, where D has been chosen as the domain height H in the simulations and as the measured boundary-layer depth δ in the wind-tunnel experiment (defined as the height at which the velocity is 99% of the free stream velocity). The displacement height d has a value $0.835h$ for the aligned array and $0.83h$ for the staggered array in both the simulations and the wind-tunnel measurements (see Section 4.4.3). In the wind tunnel, the lowest measurement point is at $z = 1.31h$ for the staggered array and at $z = 1.2h$ for the aligned array. The computed values of $\langle \overline{u'w'}\rangle^{1/2}$ are almost identical with the experimental values. The computed values of $\langle \overline{u'^2}\rangle^{1/2}$ and $\langle \overline{w'^2}\rangle^{1/2}$ are very close to the measured values for the staggered array. For the aligned array, $\langle \overline{u'^2}\rangle^{1/2}$ is slightly overestimated and $\langle \overline{w'^2}\rangle^{1/2}$ is slighly underestimated. The dispersive stresses, plotted in Fig. 16c for the aligned array, decrease rapidly with height above the array, reflecting the fact that the mean flow structure imposed by the geometry does not extend very far vertically. Note that the dispersive stresses are much smaller than the Reynolds stresses above the array
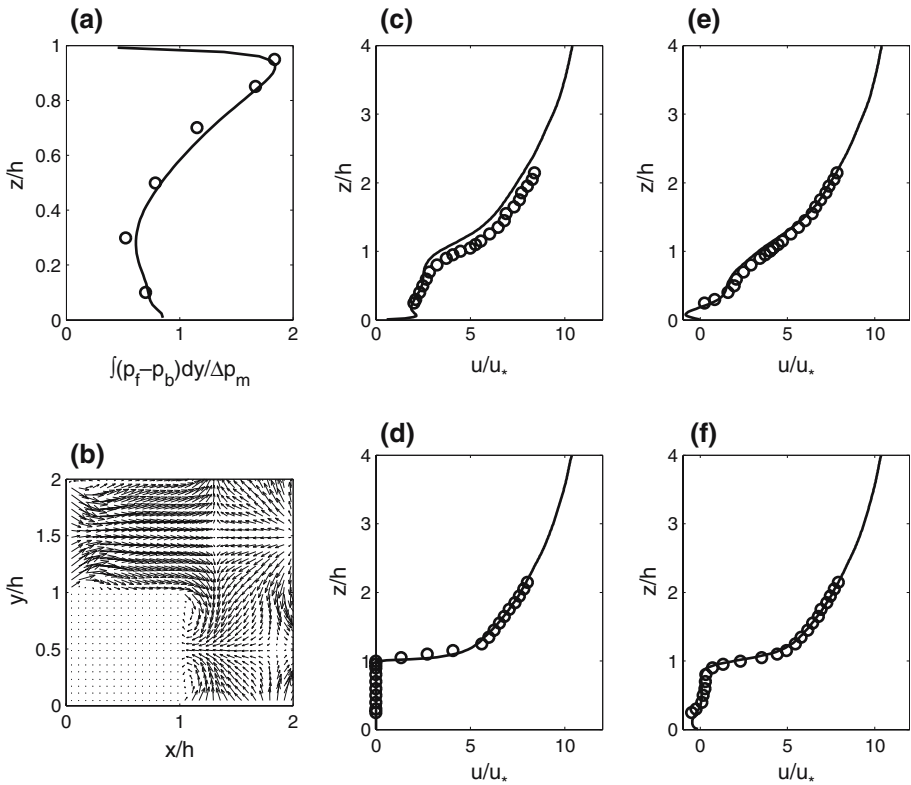
Fig. 15 (**a**) Computed vertical profile of laterally-integrated pressure difference between front and back faces of a cube in the staggered array, normalised by the pressure difference in the middle, $\int (p_f - p_b) \, dy / \Delta p_m$. (**b**) Wind vector plot of the mean wind field (u, v) in a horizontal $x - y$ plane at $z = 0.1h$ within a repeating unit in the staggered array. Vertical profiles of streamwise mean velocity u over four locations: (**c**) in gap $(0.5h, 1.5h)$, (**d**) on cube $(0.5h, 0.5h)$, (**e**) in front of cube $(1.5h, 1.5h)$, (**f**) behind cube $(1.5h, 0.5h)$. Solid lines: computations from run 444-64. Circles: Wind-tunnel data of Cheng and Castro (2002)

(being about 1% of the total stress, or 10% r.m.s). The agreement between the computed and measured dispersive stresses is impressive given how small they are. The scatter in the wind-tunnel data, and to some extent in the computations, reflects the difficulties in obtaining statistically converged estimates of dispersive stresses above the array given their small magnitudes, the need for sampling at an adequate number of locations and also for a long enough duration (see Section 4.3.2 below).

4.3.2 Spatially-averaged momentum budget and dispersive stresses

Figure 17a shows spatially-averaged stress contributions to τ_{13} computed for the staggered array. At this high Reynolds number the viscous term $\nu \partial \langle \overline{u} \rangle / \partial z$ is negligible except at the top of the cubes, where it contributes about 3% of the total stress. Above the array, practically all the stress is carried by the Reynolds term $\langle \overline{u'w'} \rangle$. The dispersive stress $\langle \tilde{u}\tilde{w} \rangle$ is negligibly small above the array.
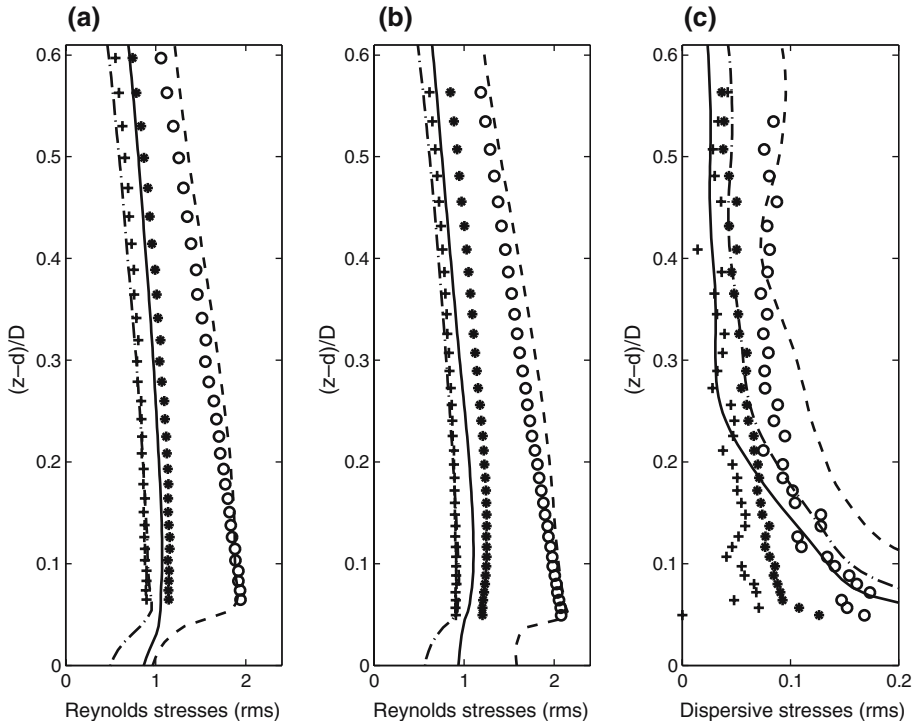
Fig. 16 Comparison of computed Reynolds and dispersive stresses with wind-tunnel data. (**a**) r.m.s. values of Reynolds stresses for staggered array, (**b**) r.m.s. values of Reynolds stresses for aligned array, (**c**) r.m.s. values of dispersive stresses for aligned array. Dot-dashed lines: $\overline{\langle u'w' \rangle}^{1/2}$ and $\langle \tilde{u}\tilde{w} \rangle^{1/2}$. Dashed lines: $\overline{\langle u'^2 \rangle}^{1/2}$ and $\langle \tilde{u}^2 \rangle^{1/2}$. Solid lines: $\overline{\langle w'^2 \rangle}^{1/2}$ and $\langle \tilde{w}^2 \rangle^{1/2}$. Symbols: Wind-tunnel data from Cheng and Castro (2002)

Figure 17b shows the computed dispersive stress above the array when a shorter averaging time is used ($50T$). Clearly the dispersive stress is then much larger. The reason for the large dispersive stress obtained with a smaller averaging time is the following. Figure 18a shows the (v, w) wind vectors in the $y - z$ plane corresponding to this averaging time. The large dispersive stress above the array is due to the presence of slow evolving mean streamwise circulations, which are very evident in Fig. 18a but which are averaged out over the much longer averaging time of $400T$ (Fig. 18b). The maximum dispersive stress occurs at about $z/h = 2$, the same height as the cores of the circulations. Such low frequency structures are commonly observed over smooth as well as rough walls (Kendall 1985; Reynolds et al. 2006), and, since they evolve slowly, they give rise to significant dispersive stresses over an interval of $50T$. Over much longer time intervals they move around and hence cease to appear as a mean spatial structure; so they do not contribute to the dispersive stresses over a very long averaging time. An averaging time substantially longer than the time scale over which they evolve is therefore necessary to achieve statistically converged results above the array; in all the runs a very long averaging time of $400T$ is therefore used. Recent experimental investigations have concluded that dispersive stresses are small above
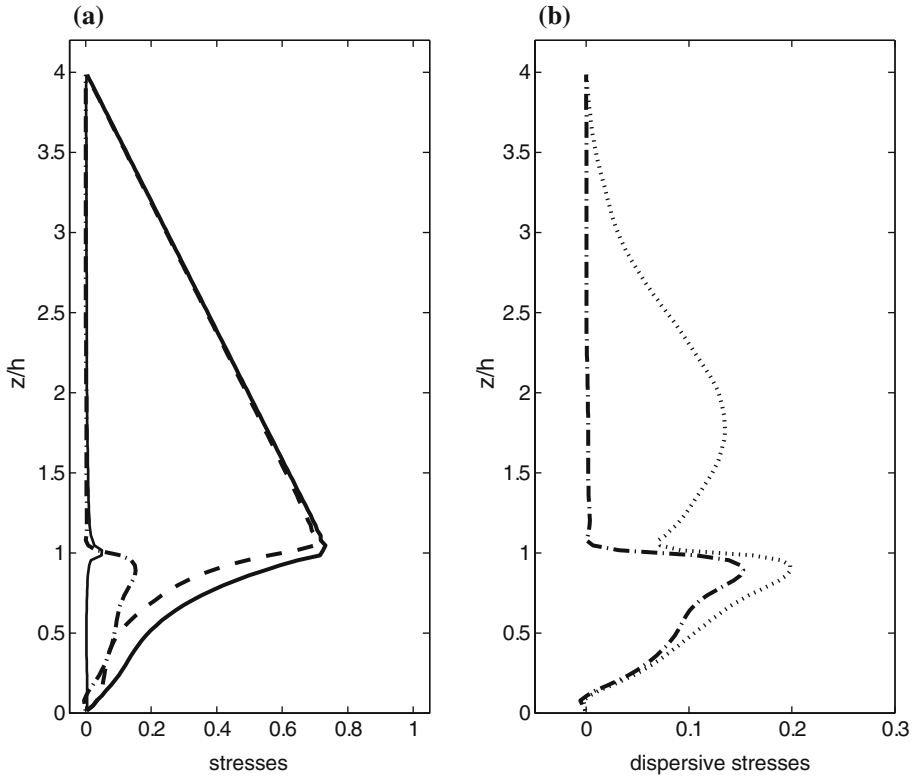
Fig. 17 (**a**) Profiles of horizontally-averaged Reynolds shear stress $\overline{\langle u'w'\rangle}$ (dashed line), dispersive stress $\langle \tilde{u}\tilde{w}\rangle$ (dot-dashed line), viscous stress $\nu\partial\langle u\rangle/\partial z$ (faint solid line) and their sum (solid line) for the staggered array, computed using an averaging time of $400T$. (**b**) Dispersive stress computed using an averaging time of $400T$ (dot-dashed line) and $50T$ (dotted line). Note the large values of the dispersive stress obtained above the array if a shorter averaging time is used

the canopy layer (Cheng and Castro 2002; Poggi et al. 2004), and the present numerical simulations confirm this.

A less well-known fact is that the magnitude of the dispersive stresses within the canopy is significant, and is especially so in the lower half of the canopy. Figure 17a shows that $\langle \tilde{u}\tilde{w}\rangle$ is comparable to or even exceeds the magnitude of the Reynolds shear stress $\overline{\langle u'w'\rangle}$ below $z = 0.5h$. This information is important for modelling the turbulence within the lower canopy. Large dispersive stresses were also found within vegetation canopies by Bohm et al. (2000) and Poggi et al. (2004).

4.3.3 Velocity fluctuations and turbulent kinetic energy

In the last section it was shown that the dispersive stress is significant in the lower half of the canopy, which means that spatial fluctuations of the mean velocity field are important there. What about temporal fluctuations from the mean? Figure 19a shows the magnitude of the computed horizontally-averaged streamwise velocity fluctuation (u') as a fraction of the horizontally-averaged mean streamwise velocity, $|\overline{\langle u'^2\rangle}^{1/2}/U|$. The solid line is for the staggered array and the dashed line is for the aligned array.
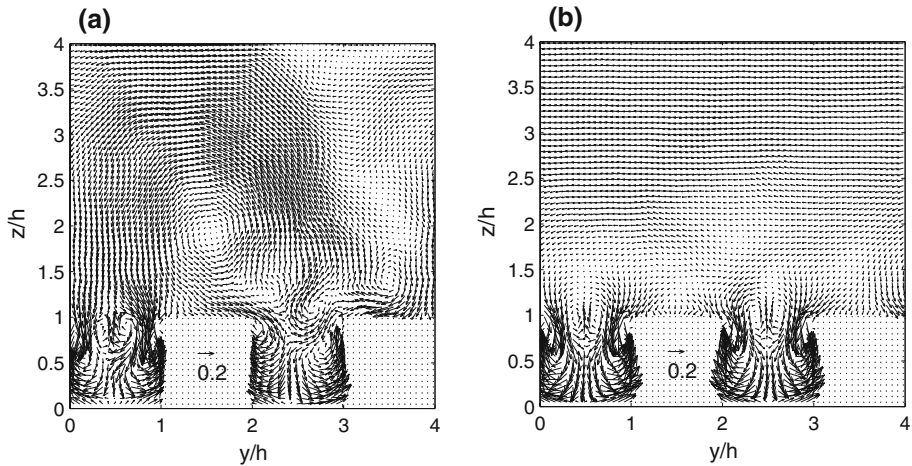
Fig. 18 (**a**) Mean velocity wind vectors of (v, w) in a $y - z$ plane through the middle of the cubes shown for a staggered array for an averaging time of $50T$. Note the presence of counter-rotating mean circulations above the cubes. (**b**) As in (**a**) but for an averaging time of $400T$. Here the streamwise circulations seen in (**a**) have been averaged out to zero

Note how this ratio increases rapidly near the bottom of the canopy. Figure 19b shows an enlarged view of the plot for the lower part of the canopy $z = 0.25h$, with the plots showing how extreme the velocity fluctuations are. For the aligned array the spatially averaged fluctuating velocity u_{rms} is up to 2.5 times the spatially averaged mean velocity U whereas it goes up to 16 times for the staggered array. Figures 19c and d plot the turbulent kinetic energy (TKE) as a fraction of the energy in the spatially-averaged mean flow, $(\langle \overline{u'^2} \rangle + \langle \overline{v'^2} \rangle + \langle \overline{w'^2} \rangle)/(U^2 + V^2 + W^2)$. Here the ratio becomes even more significant because of the contributions of the lateral and vertical fluctuations $\langle \overline{v'^2} \rangle$ and $\langle \overline{w'^2} \rangle$, whereas their mean counterparts V^2 and W^2 are of course zero. The TKE for the aligned array is up to 10 times the kinetic energy of the spatially-averaged mean flow, and for the staggered array it is up to 33 times! It is perhaps more instructive to compute the TKE as a fraction of the total energy in the mean flow, including that due to the dispersive component. Figures 19e and 19f plot the ratio $(\langle \overline{u'^2} \rangle + \langle \overline{v'^2} \rangle + \langle \overline{w'^2} \rangle)/(\langle \overline{u}^2 \rangle + \langle \overline{v}^2 \rangle + \langle \overline{w}^2 \rangle)$, where now the local mean velocity components $\overline{u_i} = U_i + \tilde{u}_i$ are used in computing the mean kinetic energy. The plots show that the TKE can be up to about 1.5 times the total energy in the mean flow in the lower canopy.

Based on these results it appears that close to the bottom of the canopy the spatially-averaged mean velocity U_i does not have much significance on its own, and that even the local mean velocity $\overline{u_i}$ can be less significant that the temporal velocity fluctuations u'_i. Therefore, when making urban measurements it is not sufficient to calculate only the mean wind speed; it is important to compute from the measurements fluctuating velocity components such as $\langle \overline{u'^2} \rangle^{1/2}$.

### 4.3.4 Influence of layout on spatially-averaged statistics

Figure 20 summarises the influence of layout on computed statistics. The solid lines are for the staggered array, dashed lines are for the aligned array and dot-dashed lines are

(a)

(b)

(c)

(d)

(e)

(f)
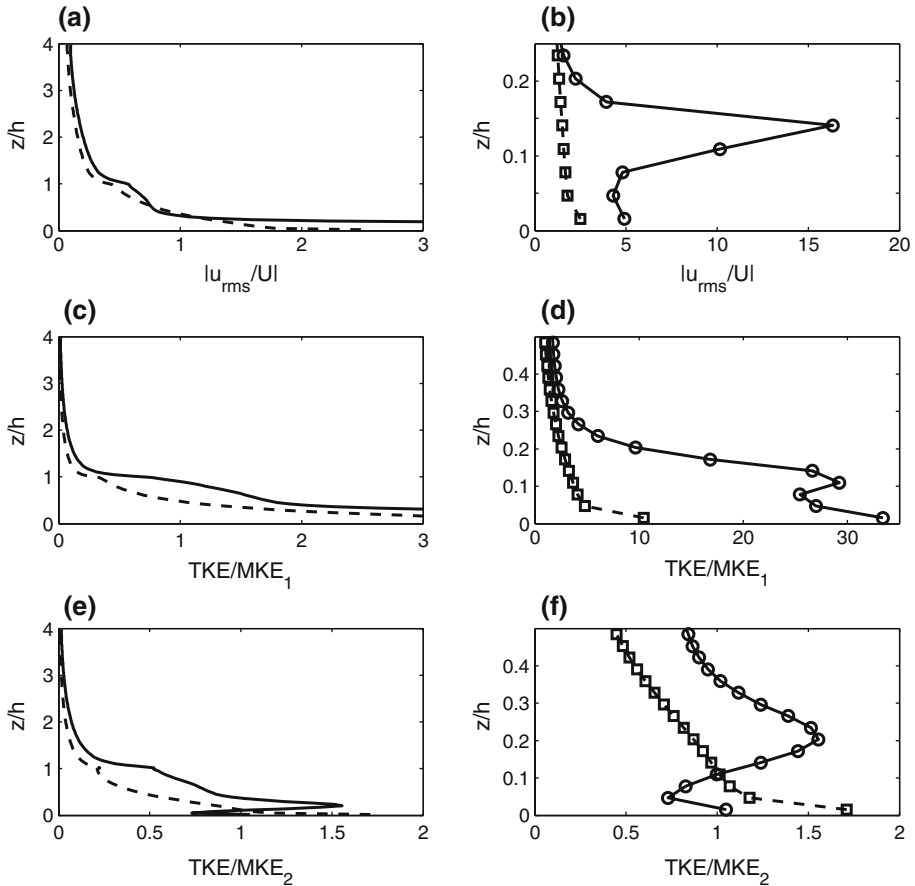
Fig. 19 (**a**) Magnitude of horizontally-averaged streamwise velocity fluctuation as a fraction of horizontally-averaged mean streamwise velocity, $|\langle \overline{u'^2} \rangle^{1/2}/U|$. (**b**) as in (**a**) for lower part of canopy. (**c**) Fraction of turbulent kinetic energy to energy in the spatially-averaged mean flow, $(\langle \overline{u'^2} \rangle + \langle \overline{v'^2} \rangle + \langle \overline{w'^2} \rangle)/(U^2 + V^2 + W^2)$. (**d**) as in (**c**) for lower part of canopy. (**e**) Fraction of turbulent kinetic energy to energy in the mean flow, $(\langle \overline{u'^2} \rangle + \langle \overline{v'^2} \rangle + \langle \overline{w'^2} \rangle)/(\langle \overline{u}^2 \rangle + \langle \overline{v}^2 \rangle + \langle \overline{w}^2 \rangle)$. (**f**) as in (**e**) for lower part of canopy. Solid line: staggered array; Dashed line: aligned array. (**c**) as in (**a**) for lower part of canopy

for the square array. The first point to note is that the plots for the aligned and square arrays are almost indistinguishable except for the streamwise turbulence intensity $\langle \overline{u'^2} \rangle$. The spanwise and vertical turbulence intensities $\langle \overline{v'^2} \rangle$ and $\langle \overline{w'^2} \rangle$ for the staggered array are very similar to those for the aligned array, but the streamwise turbulence intensity $\langle \overline{u'^2} \rangle$ is much lower within the canopy layer. Recall that the r.m.s. streamwise turbulence intensity normalised by the mean velocity is *higher* in the staggered array (Fig. 19). The reason that $\langle \overline{u'^2} \rangle$ is lower here is because of the enhanced drag of the staggered array (see Fig. 20i), which leads to a much reduced mean velocity within the staggered array (Fig. 20g).

Figure 20d–f compare the Reynolds shear stress $\langle \overline{u'w'} \rangle$, dispersive stress $\langle \tilde{u}\tilde{w} \rangle$ and total stress $\langle \overline{u'w'} \rangle + \langle \tilde{u}\tilde{w} \rangle + \nu \partial \langle u \rangle / \partial z$ for the three layouts. The main differences occur
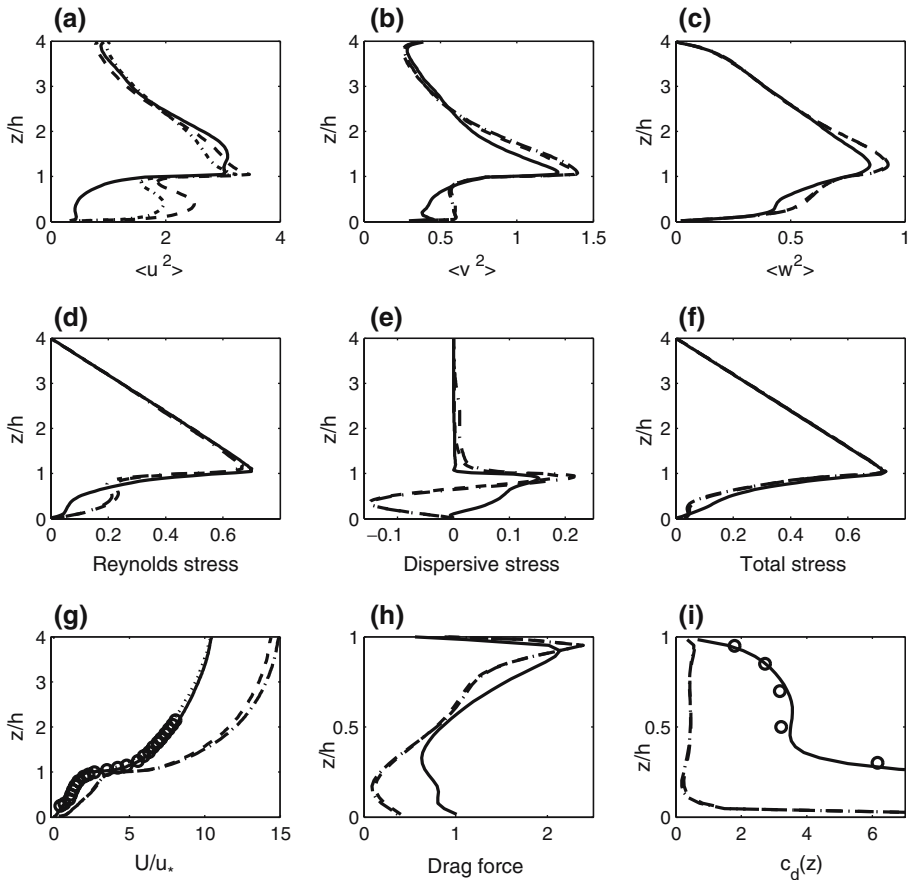
Fig. 20 Dependence of computed statistics on layout of roughness array. Solid lines: staggered array. Dashed lines: aligned array. Dot-dashed line: square array. Dotted line: spatial average of mean streamwise velocity in staggered array using only four sampling points per repeating unit. Circles: wind tunnel data from Cheng and Castro (2002) for staggered array. (**a**) $\langle \overline{u'^2} \rangle$ (**b**) $\langle \overline{v'^2} \rangle$ (**c**) $\langle \overline{w'^2} \rangle$ (**d**) shear stress $\langle \overline{u'w'} \rangle$ (**e**) dispersive stress $\langle \tilde{u}\tilde{w} \rangle$ (**f**) total stress $\langle \overline{u'w'} \rangle + \langle \tilde{u}\tilde{w} \rangle + \nu \partial \langle u \rangle / \partial z$ (**g**) horizontally-averaged mean streamwise velocity $U \equiv \langle \overline{u} \rangle$ (**h**) drag force $F_d(z)$ (**i**) sectional drag coefficient $c_d(z)$

in the lower half of the canopy, where the Reynolds stress in the staggered array is lower and the dispersive stress is higher. The profile of dispersive stress for the aligned and square arrays is qualitatively different; it changes sign at about $z = 0.6h$, due to the existence of a strong mean recirculation in these cases. Poggi et al. (2004) recently reported similar findings in wind-tunnel measurements within model plant canopies in an aligned arrangement. Note also that the dispersive stress above the staggered array is practically negligible.

The spatially-averaged mean velocity $U \equiv \langle \overline{u} \rangle$ computed for the staggered array is compared with wind-tunnel data from Cheng and Castro (2002) in Fig. 20g; the data were obtained as the average of four profiles. Therefore, a four-profile spatial average is also computed from the simulation data (shown as the dotted line), as well as the full

average obtained from all the computed profiles (the solid line). The 4-point average is remarkably close to the full average, and also agrees very well with the wind-tunnel data. Compared to the staggered array, the velocities in the aligned and square arrays are higher by about 50% above the array and 100% within, due to greater sheltering.

The fact that the three-dimensional flow structure in the staggered array is very different from that in the square or aligned arrays (see Sect. 4.2.1) leads to important differences in the profiles of pressure drag. The cubes in the staggered configuration are further apart streamwise, hence there is less sheltering. Moreover, the flow is diverted laterally because of staggered cubes in adjacent rows and speeds up in the gap, leading to greater pressure on the front face of the cubes. This happens over most of the depth of the staggered array. In contrast, the close vicinity of cubes in the square/aligned arrays and the absence of lateral flow diversion mean that most of the momentum flux arises from the top. This has the consequence that the pressure-drag profile for the staggered array is fuller, as shown in Fig. 20h.

4.4 Parameterisations

4.4.1 Drag coefficient

The sectional drag coefficient $c_d(z)$, defined by

$$\Delta p(z) = (1/2)\rho\, U^2(z)\, c_d(z), \tag{4}$$

(Macdonald 2000) is an important parameter used in distributed canopy drag models (Martilli et al. 2002; Coceal and Belcher 2004, 2005). It is difficult to obtain experimentally, but is easy to compute from the results of the simulations. Figure 20i shows the profiles of $c_d(z)$ for the three arrays. The computed $c_d(z)$ for the staggered array agrees remarkably well with that computed from the detailed wind-tunnel data of Cheng and Castro (2002). The value of $c_d(z)$ for the staggered array lies between 2 and 3 in the upper half of the canopy, then increases rapidly further down due to the small values of the mean velocity in the lower canopy. Note that the values of $c_d(z)$ for the aligned and square arrays are much smaller (by an order of magnitude) than the staggered case, due to the much higher velocities $U(z)$ as well as lower drag within these arrays, as seen in Figs. 20g and h.
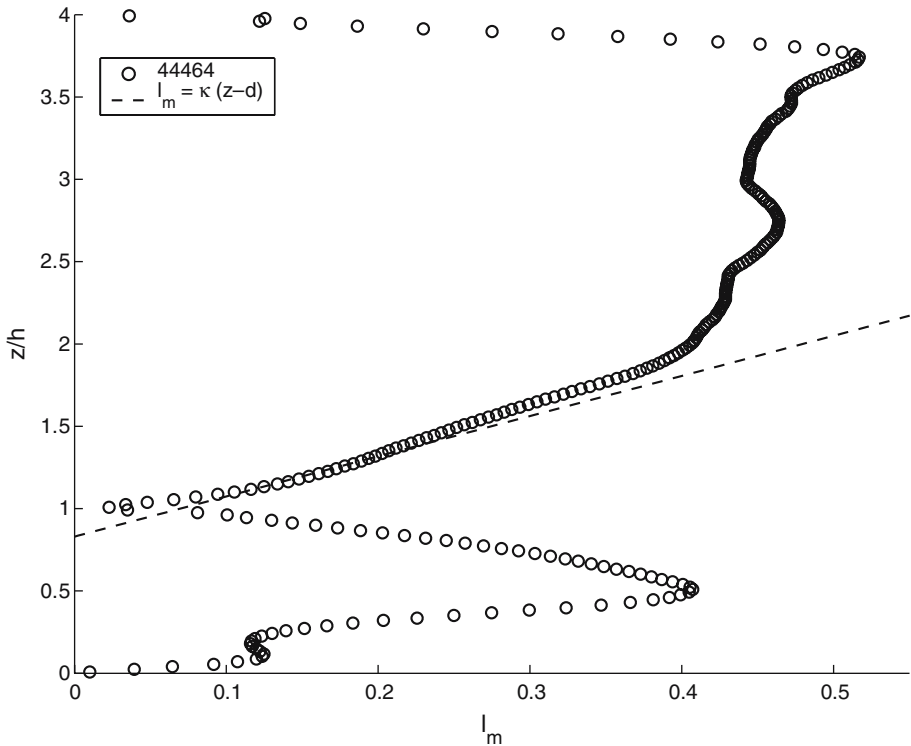
4.4.2 Effective mixing length

In addition to parameterising the drag, modellers are interested in parameterising the turbulence. The simplest turbulence closure models are formulated in terms of a mixing length. An effective, spatially-averaged mixing length defined as

$$l_m \equiv \sqrt{\langle \overline{u'w'} \rangle} \Big/ dU/dz, \tag{5}$$

may be computed from the simulation data. The profile of $l_m(z)$ is plotted in Fig. 21 for the staggered array, using data from the run 444-64.

Figure 21 shows that the mixing length increases linearly with distance above the array between approximately $z = 1.2h$ to $1.8h$, and indicates blocking of large, energetic eddies in the boundary layer above the cubes. Figure 21 also shows that the mixing length increases linearly from a small minimum value of $l_m/h \approx 0.02$ at the top of the array to a maximum of $l_m/h \approx 0.4$ at $z/h = 0.5$. It then decreases again,

Fig. 21 Effective mixing length profile computed for run 444-64. Dashed line: $l_m = \kappa \, (z - d)$. The mixing length increases linearly from a small value near the top of the array both above and below the array top. This indicates that, in an average sense, large eddies are blocked by the strong shear layer over the top of the cubes

approximately linearly, from $z/h = 0.5$ down to the surface. This variation of the mixing length contrasts with plant-like canopies consisting of tall thin roughness elements, where the mixing length is constant with depth inside the canopy (Finnigan 2000). This would again indicate that large eddies within the canopy are blocked by the top of the array, as well as by the bottom surface.

It is reasonable to suspect that the blocking layer near the top of the cubes corresponds to the average position of the strong shear layer visualised in Fig. 8 (Hunt and Durbin 1999; Belcher et al. 2003). Such a strong shear layer would resist penetration by large structures from either above or below and would tend to disrupt them (Thomas et al. 2003), thus providing a natural mechanism for blocking of eddies. There is need for caution though, since Fig. 21 is obtained from the mean velocity field and Reynolds stress. Hence, the idea of blocking by the shear layer, and the particularly small value of the mixing length at $z = h$, must be taken in a time-averaged sense. The instantaneous flow deviates significantly from the mean even near the canopy top (see Fig. 19). From an instantaneous perspective there must be intermittent penetration of large eddies from above into the canopy. This point again emphasises the risks of conceptualizing turbulence and turbulent coupling from a time-mean point of view in a highly unsteady situation.

4.4.3 Displacement height and roughness length

We describe how roughness parameters d and z_0 are determined from the spatially-averaged data above the canopy. The issue is complicated by the fact that the flow is here maintained by a constant pressure gradient.

In canopy flows, the zero-plane displacement height d is the effective height of the ground due to vertical flow displacement through the canopy (Raupach et al. 1991). A heuristic model considers d as the average height of the blocking shear layer (Belcher et al. 2003), and one may then write the linear variation of the mixing length as

$$l_m = \kappa (z - d). \tag{6}$$

Using a surface friction velocity $u_\tau (p)$ derived from form drag measurements, Cheng and Castro (2002) deduced the value of $d/h = 0.83$ by a best fit to their measured mean velocity profile. Using this value of d Eq. (6) gives a close fit to the linear part of the computed mixing length profile. This is shown as the dashed line in Fig. 21.

To derive a value for the aerodynamic roughness length z_0 one first needs to show that a logarithmic mean velocity profile exists in this pressure-driven flow, otherwise z_0 cannot be defined. This requires integrating the equation

$$l_m \, dU/dz = u_\tau \sqrt{1 - z/H}, \tag{7}$$

where the extra factor includes the linear variation of shear stress throughout the whole flow required to balance the applied streamwise pressure gradient (the dispersive and viscous stresses are negligible above the array). The last equation can be reduced to an ordinary differential equation by using the substitution $U = (u_\tau/\kappa)\sqrt{1 - d/H}f(\zeta)$, where $\zeta = (z - d)/(H - d)$. The resulting equation may then be integrated and the result expanded as a series to yield

$$U(z) = \frac{u_\tau \sqrt{1 - d/H}}{\kappa} \left[\ln\left(\frac{z - d}{z_0}\right) - \frac{1}{2}\left(\frac{z - d}{H - d}\right) + O\left(\frac{z - d}{H - d}\right)^2 \right], \tag{8}$$

where the constant of integration has been absorbed into the log term as the parameter z_0. Equation (8) shows that $U(z)$ has a logarithmic profile with zero-plane displacement d and roughness length z_0 provided that we use the shear velocity $u_\tau \sqrt{1 - d/H}$ at the height of the effective origin $z = d$ (the additional terms are small near the top of the array). This then defines an effective u_* for a pressure-driven channel flow, and gives a basis for making a comparison with a constant stress system. A consequence of the above analysis is that any straight line on the graph of z/h vs. l_m corresponds to a logarithmic velocity profile with the corresponding values of κ and d; hence fitting a log profile is equivalent to fitting the mixing length. Using the values $u_* = u_\tau \sqrt{1 - d/H}$ with $d/h = 0.83$ gives a best fit roughness length of $z_o/h = 0.045$, close to the value of 0.053 which Cheng and Castro deduced by best-fitting a log profile to their measured mean velocity data.

Jackson (1981) has proposed a different interpretation of the zero-plane displacement in which d is the effective height at which the form drag acts,

$$d = \int_0^h zD(z)\,dz \bigg/ \int_0^h D(z)\,dz. \tag{9}$$

This may be evaluated with the present data and results in a smaller value $d/h = 0.60$. The semi-empirical expression proposed by Macdonald et al. (1998) relating d/h for staggered arrays of cubes to the *plan area density* λ_p (here $= 0.25$), $d/h = 1 - 4.43^{-\lambda_p}(1 - \lambda_p)$ gives $d/h = 0.48$, which is even smaller. Hence, one should note that these three ways of obtaining the zero-plane displacement are not consistent with one another.

5 Conclusions

The good agreement achieved between the present simulations and wind-tunnel data shows the promise of the method for generating comprehensive datasets that may be used for validating simpler models, such as urban canopy models (Coceal and Belcher 2004, 2005) or LES at lower resolutions (Xie and Castro submitted). Valuable information of use to modellers such as drag coefficients and further statistics such as the terms of the turbulent kinetic energy budget can be computed.

The results have shown the important influence of building layout, both on the mean flow structure and on the turbulence statistics. This finding highlights in particular the need to consider the three dimensionality of the flow. By implication, models of urban areas based exclusively on two-dimensional street canyon representations may be missing important aspects of the flow around actual three-dimensional buildings. Indeed, one would like to take things one step further. The arrays we have investigated are closely packed and of uniform height, which are both conducive to the formation of a strong and continuous shear layer; the effect of packing density and variable height is an important subject for future investigation.

Another important finding is that unsteady effects are significant and cannot be ignored, especially in the lower canopy. It is common in the literature on urban canopy flows for discussions to be based on a mean picture of the flow; this may be misleading. Applications that depend on the flow dynamics on short time scales, such as the dispersion of pollutants, may require a much more detailed understanding of the unsteady flow. Simulations like those presented in this paper allow one to probe the unsteady dynamics in great detail. Some aspects of this, including an investigation of organised features of the turbulence over cubical roughness arrays, are reported in Coceal et al. (submitted).

Finally, this work is able to shed light on turbulence over rough surfaces in general. Representing a generic rough surface by means of geometrically regular roughness such as the present cubical arrays makes it possible to perform direct numerical simulations. The fact that the flow within the actual roughness is resolved in detail can also reveal a great deal about canopy flows. There are at least two paradigms here. First, we might consider the roughness elements to be obstacles, so that the flow within and above the roughness elements is formed by the interacting wakes of the obstacles. Second, the canopy of roughness elements can be considered as a porous medium that exerts an aerodynamic drag on the flow. Investigations of atmospheric boundary-layer flow over vegetation and forest canopies have taken this approach (Finnigan 2000), and shown that the inflection point in the mean velocity profile at the top of the canopy leads to a mixing layer instability that produces large eddies that control the mixing within and immediately above the canopy. A subject of continuing investigation is whether a similar or a different mechanism operates for urban-like canopies.

References

Belcher SE (2005) Mixing and transport in urban areas. Phil Trans Roy Soc 363:2947–2963

Belcher SE, Jerram N, Hunt JCR (2003) Adjustment of the atmospheric boundary layer to a canopy of roughness elements. J Fluid Mech 488:369–398

Bohm M, Finnigan JJ, Raupach MR (2000) Dispersive fluxes in canopy flows: just how important are they? Proc 24th conference on agricultural and forest meteorology, American Meteorological Society, Davis, CA

Britter RE, Hanna SR (2003) Flow and dispersion in urban areas. Annu Rev Fluid Mech 35:469–496

Castro IP, Robins AG (1977) The flow around a surface-mounted cube in uniform and turbulent streams. J Fluid Mech 79:307–335

Castro IP, Cheng H, Reynolds R (2006) Turbulence over urban-type roughness: deductions from wind tunnel measurements. Boundary-Layer Meteorol 118:109–131

Cheng H, Castro IP (2002) Near wall flow over urban-like roughness. Boundary-Layer Meteorol 104:229–259

Coceal O, Belcher SE (2004) A canopy model of mean winds through urban areas. Quart J Roy Meteorol Soc 130:1349–1372

Coceal O, Belcher SE (2005) Mean winds through an inhomogeneous urban canopy. Boundary-Layer Meteorol 115:47–68

Cui et al. (2004) Large-eddy simulation of turbulent flow in a street canyon. Quart J Roy Meteorol Soc 130:1373–1394

Delery JM (2001) Robert Legendre and Henri Werle: Toward the elucidation of three-dimensional separation. Annu Rev Fluid Mech 33:129–154

Djenidi L, Elvarasan R, Antonia RA (1999) The turbulent boundary layer over transverse square cavities. J Fluid Mech 395:271–294

Finnigan JJ (1985) Turbulent transport in flexible plant canopies. In: Hutchinson BA, Hicks BB (eds) The Forest-Atmosphere Interaction

Finnigan JJ (2000) Turbulence in plant canopies. Annu Rev Fluid Mech 32:519–572

Hamilton JM, Kim J, Waleffe F (1995) Regeneration mechanisms of near-wall turbulence structures. J Fluid Mech 287:317–348

Hanna SR, Tehranian S, Carissimo B, Macdonald RW, Lohner R (2002) Comparisons of model simulations with observations of mean flow and turbulence within simple obstacle arrays. Atmos Environ 36:5067–5079

Hunt JCR, Durbin PA (1999) Perturbed vortical layers and shear sheltering. Fluid Dyn Res 24:375–404

Jackson PS (1981) On the displacement height in the logarithmic profile. J Fluid Mech 111:15–25

Jimenez J, Pinelli A (1999) The autonomous cycle of near-wall turbulence. J Fluid Mech 389:335–359

Jimenez J (2004) Turbulent flows over rough walls. Annu Rev Fluid Mech 36:173–196

Kanda M, Moriwaki R, Kasamatsu F (2004) Large-eddy simulation of turbulent organized structures within and above explicitly resolved cube arrays. Boundary-Layer Meteorol 112:343–368

Kendall JM (1985) Experimental study of disturbances produced in pre-transitional laminar boundary layer by weak free stream turbulence. AIAA Paper:85–1695

Leonardi S, Orlandi P, Smalley RJ, Djenidi L, Antonia RA (2003) Direct numerical simulations of turbulent channel flow with transverse square bars on one wall. J Fluid Mech 491:229–238

Macdonald RW, Griffiths RF, Hall DJ (1998) An improved method for the estimation of surface roughness of obstacle arrays. Atmos Environ 32:1857–1864

Macdonald RW (2000) Modelling the mean velocity profile in the urban canopy layer. Boundary-Layer Meteorol 97:25–45

Martilli A, Clappier A, Rotach MW (2002) An urban surface exchange parameterisation for mesoscale models. Boundary-Layer Meteorol 104:261–304

Martinuzzi R, Tropea C (1993) The flow around surface-mounted, prismatic obstacles placed in a fully-developed channel flow. J Fluids Eng 115:85–92

Moin P, Mahesh K (1998) Direct numerical simulation: a tool in turbulence research. Annu Rev Fluid Mech 30:539–578

Pao TH (1965) Structure of turbulent velocity and scalar fields at large wave numbers. Phys Fluids 8:1063

Poggi D, Katul GG, Albertson JD (2004) A note on the contribution of dispersive fluxes to momentum transfer within canopies. Boundary-Layer Meteorol 111:615–621

Raupach MR, Shaw RH (1982) Averaging procedures for flow within vegetation canopies. Boundary-Layer Meteorol 22:79–90

Raupach MR, Antonia RA, Rajagopalan S (1991) Rough-wall turbulent boundary layers. Appl Mecha Rev 44:1–25.

Reynolds RT, Hayden P, Castro IP, Robins AG (2006) Spanwise variations in nominally two-dimensional rough-wall boundary layers. Expts Fluids In press

Snyder WH, Castro IP (2002) The critical Reynolds number for rough-wall boundary layers. J Wind Eng Ind Aerodyn 90:41–54

Stoesser T, Mathey F, Frohlich J, Rodi W (2003) LES of flow over multiple cubes. ERCOFTAC Bull No. 56

Thomas TG, Yao YF, Sandham ND (2003) Structure and energetics of a turbulent trailing edge flow. Comput Math Appl 46:671–680

Tobak M, Peake DJ (1982) Topology of three-dimensional separated flows. Annu Rev Fluid Mech 14:61–85

Yao YF, Thomas TG, Sandham ND, Williams JJR (2001) Direct numerical simulation of turbulent flow over a rectangular trailing edge. Theoret Comput Fluid Dyn 14:337–358